Photoelectron angular distributions of H ionization in low energy regime: Comparison between different potentials*

Shu-Na Song(宋舒娜)[1], Hao Liang(梁昊)[1], Liang-You Peng(彭良友)[1,2], and Hong-Bing Jiang(蒋红兵)[1,2,†]

[1] *State Key Laboratory for Mesoscopic Physics and Collaborative Innovation Center of Quantum Matter, School of Physics, Peking University, Beijing* 100871, *China*

[2] *Collaborative Innovation Center of Extreme Optics, Shanxi University, Taiyuan* 030006, *China*

(Received 11 April 2016; revised manuscript received 15 May 2016; published online 2 August 2016)

We theoretically investigate the low energy part of the photoelectron spectra in the tunneling ionization regime by numerically solving the time-dependent Schrdinger equation for different atomic potentials at various wavelengths. We find that the shift of the first above-threshold ionization (ATI) peak is closely related to the interferences between electron wave packets, which are controlled by the laser field and largely independent of the potential. By gradually changing the short-range potential to the long-range Coulomb potential, we show that the long-range potential's effect is mainly to focus the electrons along the laser's polarization and to generate the spider structure by enhancing the rescattering process with the parent ion. In addition, we find that the intermediate transitions and the Rydberg states have important influences on the number and the shape of the lobes near the threshold.

Keywords: low energy, tunneling ionization, Coulomb potential, Rydberg states

PACS: 32.80.Rm, 42.50.Hz, 42.65.Re **DOI:** 10.1088/1674-1056/25/9/093201

1. Introduction

In the investigation of light–matter interactions in the strong fields, the photoelectron angular distributions and the photoelectron spectra provide abundant information about the ionization dynamics which reflects the information about the laser field and the target structure. For a given ionization potential I_p which is much larger than the photon energy, Keldysh[1] divided the ionization into the multi-photon regime (MPI, $\gamma \gg 1$) and the tunnelling regime (TI, $\gamma \ll 1$), where the Keldysh parameter $\gamma = \sqrt{I_p/2U_p}$ with $U_p = F_0^2/4\omega^2$ being the ponderomotive energy of an electron in the laser field (F_0 is the field amplitude and ω the laser frequency). One can qualitatively understand these two ionization regimes in view of the wave-particle duality of light. In the TI regime, the wave character of the laser is mainly reflected. The electrons tunnel through the Coulomb barrier which is suppressed by the laser field and the ionization mostly happens close to the maxima of the electric field. The dominant structures observed in the photoelectron spectra can be explained as interferences between electron wave packets emitted at different times within the laser pulse. While, in the MPI regime, the particle character of light is dominant. The electron absorbs a number of photons to exceed the ionization threshold and the structures in the photoelectron spectra reflect characters of multiphoton transitions.

In recent years, the low energy structure produced by intense long-wavelength lasers (which is called ionization surprise) has drawn a great deal of attention from experimentalists and theorists. The appearance of the low energy structure can be attributed to the effects of the Coulomb potential during the multiple rescattering of the ionized electron which is ignored in the strong field approximation (SFA).[2–4] It shows the influence of ion structure on the photoelectron spectra in the TI regime and gives instructions to obtain holographic structures that record the spatial and temporal information for both the target ion and the electron.[5–8] The holographic structure (usually called "spider structure") is generated by the interference between the laser-driven electron wave packet that scatters off the target ion and the electron wave packet that does not interact with the ion. It is a large scale feature that can span multiple above threshold ionization (ATI) rings. At the same time, a radial fan-like pattern has been observed in the angular distribution in the near threshold ionization both experimentally and theoretically.[9–11,14,15] The number of near-threshold radial lobes was suggested to be determined by the minimum number of photons needed to ionize the atom[15] and an empirical rule was given for the dominant orbital angular momentum. Latter, using a classical trajectory Monte Carlo method (CTMC), Arbó *et al*. quantitatively explained the dominant orbital angular momentum in terms of interfering classical trajectories in the presence of both the Coulomb and laser fields.[9,10] The study of photoelectron angular distributions of near zero momentum is generally related to the recapture of electrons into Rydberg states.[14] However, the CTMC method ignores the intermediate transition processes since the ionization rate is prescribed by the Ammosov–Delone–Krainov

*Project supported by the National Natural Science Foundation of China (Grant Nos. 11322437 and 11574010) and the National Basic Research Program of China (Grant No. 2013CB922402).

†Corresponding author. E-mail: hbjiang@pku.edu.cn

© 2016 Chinese Physical Society and IOP Publishing Ltd

(ADK) theory, which only considers the transition rates from the bound state to the continuum states.[16,17] The comparison between TDSE calculation and the semi-classical model within a wide range of laser parameters shows the limit of its applicability.[8]

In this paper, we investigate the photoelectron angular distributions of the ionization of a hydrogen atom by solving the time-dependent Schrdinger equation (TDSE) in the TI regime with intense infrared (IR) laser pulses. We find that the shift of the first ATI ring in the momentum distribution with the changing of the wavelength reflects the interference of electron wave packets under the control of a laser field, which is largely independent of the used potential. The influences of the long-range Coulomb potential and excited states on photoelectron angular distributions are studied by changing the Yukawa potential's parameter. By gradually changing the short potential to the long-range Coulomb potential, we can see the "spider structure" is gradually reproduced. In addition, the number of lobes and the radial pattern on the near threshold ring (first ATI ring or below the first ATI ring) is connected with the increase of the number of excited states when one changes the Yukawa potential's parameter.

The organization of the rest of this paper is as follows. In Section 2, the numerical method is described in brief. In Section 3, we present our main results and discussion. Section 4 is a short summary.

2. Therical methods

Our method is based on the numerical solution to the TDSE, whose details can be found in previous work.[21–24] In this work, the hydrogen in its ground 1s state is exposed to a linearly polarized laser pulse, with a vector potential given by

$$\boldsymbol{A}_L(t) = \widehat{z} A_0 f_L(t) \sin[\omega(t)], \tag{1}$$

where A_0 is the peak value of the vector potential, and we take the pulse envelope $f_L(t) = \cos^2(\pi t/\tau)$ with τ being the total pulse duration. The corresponding electric field is given by $\boldsymbol{E}_L(t) = -\partial \boldsymbol{A}_L(t)/\partial t$. In brief, the TDSE

$$\mathrm{i}\frac{\partial}{\partial t}\Psi(\boldsymbol{r},t) = \left[-\frac{1}{2}\nabla^2 + V(r) + \boldsymbol{p}\cdot\boldsymbol{A}_L(t)\right]\Psi(\boldsymbol{r},t), \tag{2}$$

is numerically solved in the spherical coordinates with the finite difference method. Two types of atomic potentials are considered, i.e., $\mathrm{V}(r) = -1/r$ for the Coulomb potential case and $V(r) = -Z\mathrm{e}^{-\kappa r}/r$ for the Yukawa potential case. The probability of a photoelectron with an asymptotic momentum $\boldsymbol{k}$ can be obtained by a projection of the final wave function $\Psi(\boldsymbol{r},t_f)$ onto the scattering states of the field-free Hamiltonian, i.e.,

$$P(\boldsymbol{k}) = P(k,\theta,\phi) = |\langle \Psi_{\boldsymbol{k}}^{-}(\boldsymbol{r})|\Psi(\boldsymbol{r},t_f)\rangle|^2, \tag{3}$$

where

$$\Psi_{\boldsymbol{k}}^{-}(\boldsymbol{r}) = \frac{1}{\sqrt{2\pi k}}\sum_{l,m}\mathrm{i}^l\,\mathrm{e}^{-l(\sigma_l+\delta_l)}Y_{lm}^*(\theta,\phi)R_{kl}(r)Y_{lm}(\theta',\varphi'), \tag{4}$$

with (θ',φ') denoting the angles of $\boldsymbol{r}$. For a linearly polarized pulse considered in the present work, $P(\boldsymbol{k})$ has an azimuthal symmetry about ϕ. The total ionization probability can then be calculated by integrating in the momentum space as

$$P_{\mathrm{total}} = 2\pi\int P(k,\theta,\phi=0)k\,\mathrm{d}k\,\mathrm{d}\theta. \tag{5}$$

3. Numerical results and discussion

In this section, we first calculate the photoelectron spectra in the TI regime with different laser wavelengths. Then, we fix the laser parameter and gradually change the Yukawa potential to approach the shape of the Coulomb potential. By comparing with the calculations using the Coulomb potential, we can evaluate the roles of the long-range Coulomb potential and intermediate states in the photoelectron angular distributions. Atomic units are used throughout.

3.1. Dependence on the laser wavelength

In our previous work,[24] we have extended the electron wave packet interference from two single-cycle pulses to one multicycle pulse, and verified that the ionization yield can be modulated by varying the wavelength. In Figs. 1 and 2, for an 8-cycle pulse at a fixed peak intensity, we present the momentum distributions at the maximum and minimum in the ionization yield for six wavelengths, using the Coulomb potential and the Yukawa potential (with $Z = 1.91$ and $\kappa = 1$ to reproduce the ionization potential of H atom) respectively. One notes that, when the total ionization yield is maximum, the first ATI ring starts from the zero point and the size of the ring is larger. When the ionization yield reaches its minimum, the first ATI ring is the second concentric ring in the momentum spectra and a smaller ring appears near the zero point. For the results of the short-range Yukawa potential in Fig. 2, the position shift of the ATI ring with the wavelength is still the same as that in the case of the Coulomb potential. This observation shows that the position shift of the first ATI ring is independent of the long-range Coulomb potential. It attributes to the electron wave packets interference, which is related to the ionization modulation. This phenomenon can be explained by the channel closing theory.[18,19] For a fixed peak intensity, if the wavelength satisfies the condition that $(|I_{\mathrm{p}}| + U_{\mathrm{p}})/\hbar\omega$ is an integer, then a new ionization channel will be opened near the zero momentum. The emitted photoelectrons have energies

$$E_n = n\hbar\omega - |I_{\mathrm{p}}| - U_{\mathrm{p}}, \tag{6}$$

and the total ionization yield will be enhanced and appears to be a maximum (note that this newly opened channel will

enhance the high energy part as well, but the probability is relatively several order lower than the first ATI ring). The three wavelengths with maximum ionization probability correspond to channels absorbing 26, 27, 28 integer numbers of photons from the laser field according to Eq. (6). In this way, we can explain the common feature using two kinds of potentials that the size fluctuation with the wavelength of the first near zero ring on the momentum spectra mainly depends on the channel closing which can be viewed as the interference of different "quantum trajectories".

Comparing Fig. 1 with Fig. 2 carefully, there are several differences in the structure of the momentum distribution. For Fig. 1, the effect of Coulomb focusing is rather obvious in that the distribution is concentrated along the laser's polarization direction (z axis) and we can also see the spider structure along the z axis. The lobes of the first ring are radial from the center and the tail of the lobes gradually changes its direction to nearly parallel to the x axis. For Fig. 2, there are mainly two structures, the interference of different cycles which results in the ATI ring and the interference between sub-cycles which leads to the rings centered on the z axis. The lobes on the first ring are all nearly parallel to the x axis which can be explained as the superposition of the two interference structures. The interference structures in Fig. 2 are less complex than those in Fig. 1, and their main structures are in fact quite similar. To achieve a clear analysis, we turn to the strong field approximation (SFA) theory. For the electron wave packets generated at t_1 and t_2, their interference pattern is determined by the phase difference accumulated in the laser field,[26]

$$\Delta S = \int_{t_1}^{t_2} \mathrm{d}\tau \left\{ 1/2[\boldsymbol{k} + \boldsymbol{A}(\tau)]^2 + I_\mathrm{p} \right\}. \tag{7}$$

The laser we use is linearly polarized along the z axis, so the position of the interference maxima can then be expressed as

$$k_x^2 + \left(k_z + \frac{F}{\Delta t} \right)^2 = R^2, \tag{8}$$

where $\Delta t = t_2 - t_1$, $F = \int_{t_1}^{t_2} \mathrm{d}\tau A(\tau)$, and R is a constant related to the laser's parameter and I_p. When $F = 0$, the interference patterns are a series of circles centered on the zero point, which are the ATI rings. When $F \neq 0$, the interference circles are centered on the z axis. The mixture of interference circles center on $k_z > 0$ and $k_z < 0$ results in the lobes on the first ATI ring nearly parallel to the x axis. Our interference analysis can be confirmed by the SFA calculation in Ref. [28].

According to the above analysis, one can also explain the main interference structures in Fig. 2, which also exist in Fig. 1. The main structure is related to the laser parameters and is a reflection of wave characteristics of the field. The subtle differences on the interference structure can be attributed to the different potentials.

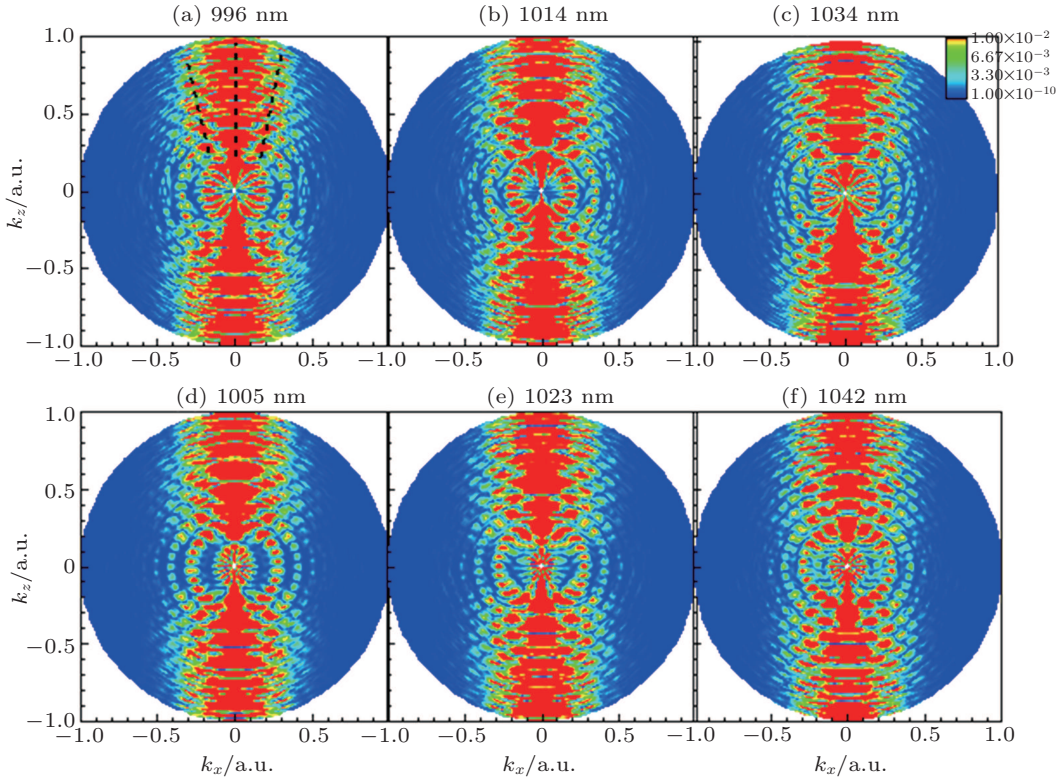


Fig. 1. (color online) Photoelectron momentum distributions on the log scale for different wavelengths, calculated for the Coulomb potential. The laser has a total duration of 8 cycles at a fixed peak intensity of $I_0 = 2 \times 10^{14}$ W/cm^2. The wavelengths are marked on the top of each panel. Panels (a)–(c) are for the case with the maximum ionization yield and panels (d)–(f) are for the minimum ionization yield, as discussed in Ref. [24]. The "spider" structures are marked with black dashed lines for guiding the eye.

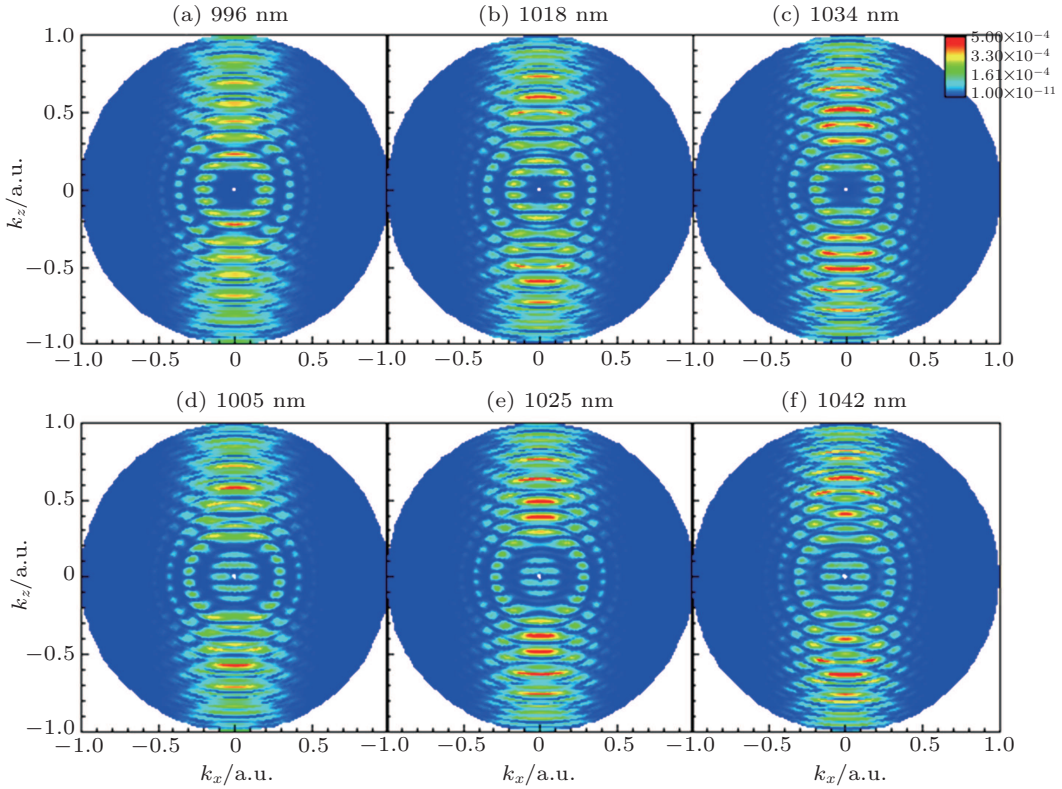


Fig. 2. (color online) The same as those Fig. 1, but calculated for the Yukawa potential with $Z = 1.91$ and $\kappa = 1$ to reproduce the ionization potential of H atom. Panels (a)–(c) are for the case with the maximum ionization yield and panels (d)–(f) are for the minimum ionization yield, as discussed in Ref. [24].

In this way, we can see the main structure of the photoelectron spectra is greatly influenced by the laser field (the strength of electric field and the frequency). It is a character for the TI regime since the tunneling electrons are mainly emitted at the peak of the field and the generated electron wave packets at different subcycles interfere with each other. The position of the ATI ring is the reflection of this interference controlled by a laser field, while the lobes of the ring which are different for the Yukawa potential and the Coulomb potential show the inner structure of the atoms. Hereafter, we will change the potential shape and the number of excited states to see the effects of the long-range potential and intermediate transitions.

3.2. Effects of intermediate transitions and long-range potential

The importance of the long-range Coulomb potential in the low energy momentum spectra has been studied in previous works.[15,27] Here, we would like to study to what extent the long-range Coulomb potential effects the shape of the first ring and the number of the lobes. For this purpose, we gradually change the Yukawa potential to a long-range potential by adjusting the parameters Z and κ to reproduce the ground state energy of the H atom. The potentials with different parameters as a function of r are shown in Fig. 3. For the potential with $\kappa = 0.45$–0.02, there are one to five bound states, respectively. As we can see, for the cases of $\kappa = 0.1$ to 0.02, there is little difference from the shape of the Coulomb potential.

Table 1. The energy levels (in a.u.) of excited states with different values of Yukawa potential.

n	κ=0.3	κ=0.15	κ=0.1	κ=0.05	κ=0.02
2	–0.0093	–0.0458	–0.0662	–0.0920	–0.1108
3			–0.0059	–0.0226	–0.0399
4				–0.0039	–0.0162
5					–0.0057

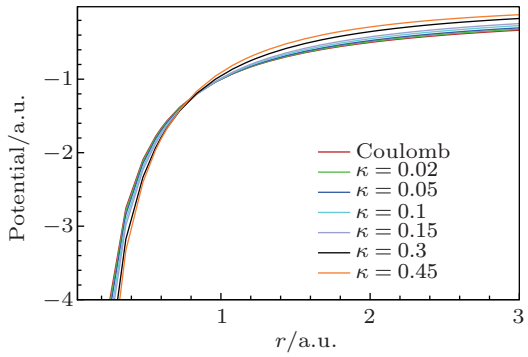


Fig. 3. (color online) The Yukawa potentials with different parameters, compared with the Coulomb potential.

We select six Yukawa potentials as shown in Fig. 3 to carry out calculations at 996 nm and 1005 nm with other laser parameters the same as those in Fig. 1. The shape of potential is gradually approaching the Coulomb potential with the decrease of parameter κ. The calculated results are shown in Figs. 4 and 5. In Table 1, we show the energy levels of the Yukawa potential with different parameters. In Figs. 4(a) and 4(b) (Figs. 5(a) and 5(b)), the interference structures are

quite the same while the main difference is the ionization yield which can be seen from the color bars. The bound states increase by one from Fig. 4(b) to Fig. 4(a) (from Fig. 5(b) to Fig. 5(a)), but these two potentials are less similar to the Coulomb potential than the other four. In Fig. 4(c) (Fig. 5(c)), the ionization yield is dramaticlly enhanced with the same number of bound states as Fig. 4(b) (Fig. 5(b)) but the Yukawa potential is more approaching the long-range potential. In addition, the signal is more concentrated to the z axis with the decrease of κ. It is interesting to see that changing the short-range potential to a long-range potential does not increase the number of lobes on the first ring but the lobe's shape gradually changes. In Figs. 4(c)–4(f) (Figs. 5(c)–5(f)), in which case the potential's shape is much closer to the Coulomb potential, the momentum distribution concentrates along the laser field which is the effect of the Coulomb focusing and the spider structure is visible along the z axis.

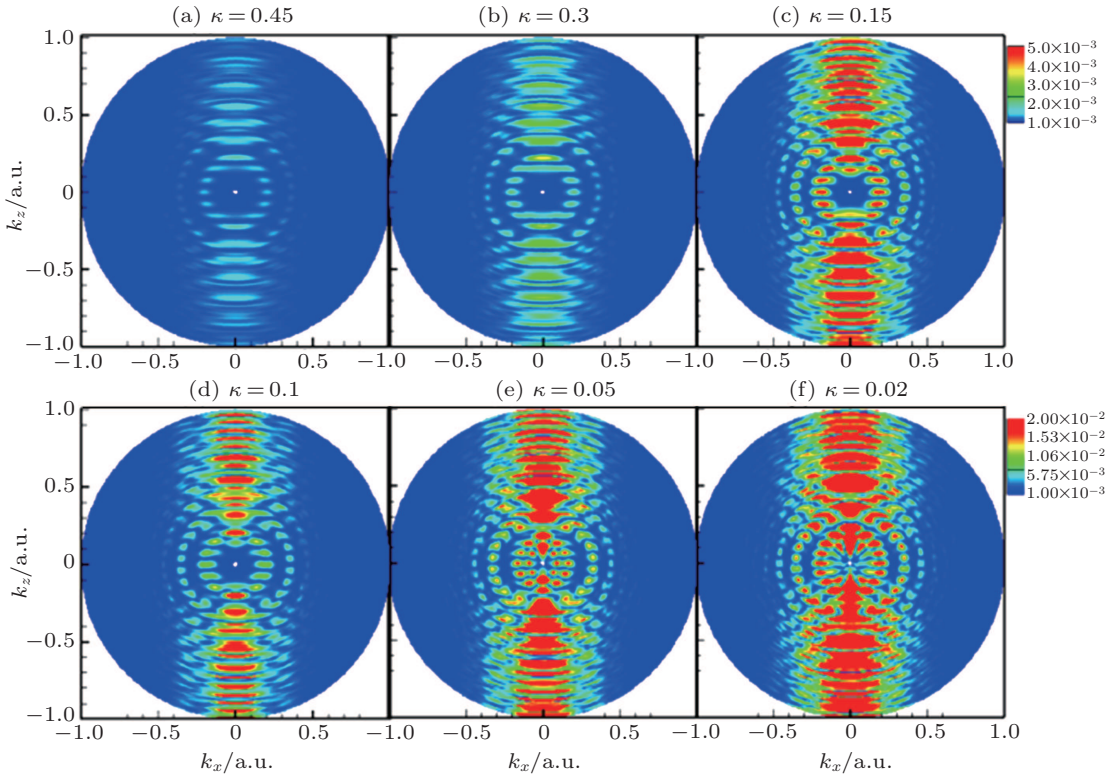


Fig. 4. (color online) Photoelectron momentum distributions at 996 nm, with the laser parameters the same as those in Fig. 1, calculated for Yukawa potentials with different parameters: (a) $\kappa = 0.45$, (b) $\kappa = 0.3$, (c) $\kappa = 0.15$, (d) $\kappa = 0.1$, (e) $\kappa = 0.05$, (f) $\kappa = 0.02$. The number of bound states from panels (a) to (f) is 1, 2, 2, 3, 4, and 5 respectively. For better visibility, different color bars are used for the first and the second rows.

The number of excited states used in Figs. 4(d)–4(f) (Figs. 5(d)–5(f)) increases from 3 to 5. From Fig. 4(f) (Fig. 5(f)), we can see the lobes on the first ring generally stretch to zero, which become similar to the result of the Coulomb potential. More importantly, the number of the lobes on the first ring also increases in Fig. 4(f) (Fig. 5(f)). It is generally accepted that the off-axis component is a reflection of the orbital angular momentum of the intermediate Rydberg state.[12,13] The electrons are first excited to an intermediate Rydberg level and then ionized by absorbing one or more photons. As we decrease the parameter κ, the potential and bound states both change and the radial structures gradually appear. One can see that the radial structure which stems from the zero center is a result of resonant ionization and the long-range potential. The lobes on the ATI ring can also be regarded as a result of the interference on the photoelectron angular distribution, which has been investigated before.[9,10,28,29] However, whether the number of lobes is controlled by the absorbed-photon number is still a question in the TI regime. According to the work in Ref. [9], they had fixed a simple relation between the angular momentum L and quiver amplitude, which is a function of the momentum $\boldsymbol{k}$. This semi-classical model will lose its efficacy as the laser intensity is increased,[11] which is the case in our work. We find that the predicted number of the lobes is larger than the TDSE results.

As we change the Yukawa potential to the long-range potential, the number of excited states does not change in a linear fashion with the shape of potential since the excited states become more and more denser near the continuum states. It shows that the combined effect of a series of Rydberg states plays an important role in the formation of a different num-

ber of the radial lobes near the zero momentum. One can obtain the momentum distribution by projecting the final wave function onto the scattering states. The scattering states are a description of the electron's scattering by the Coulomb potential, and the projection can be expanded into a series of spherical harmonics. The l means different scattering trajectories that the electrons are emitted from different initial states or experienced the scattering process, but these trajectories do not accurately describe the quantum states when the tunneling electrons recombine with the ion after the scattering.

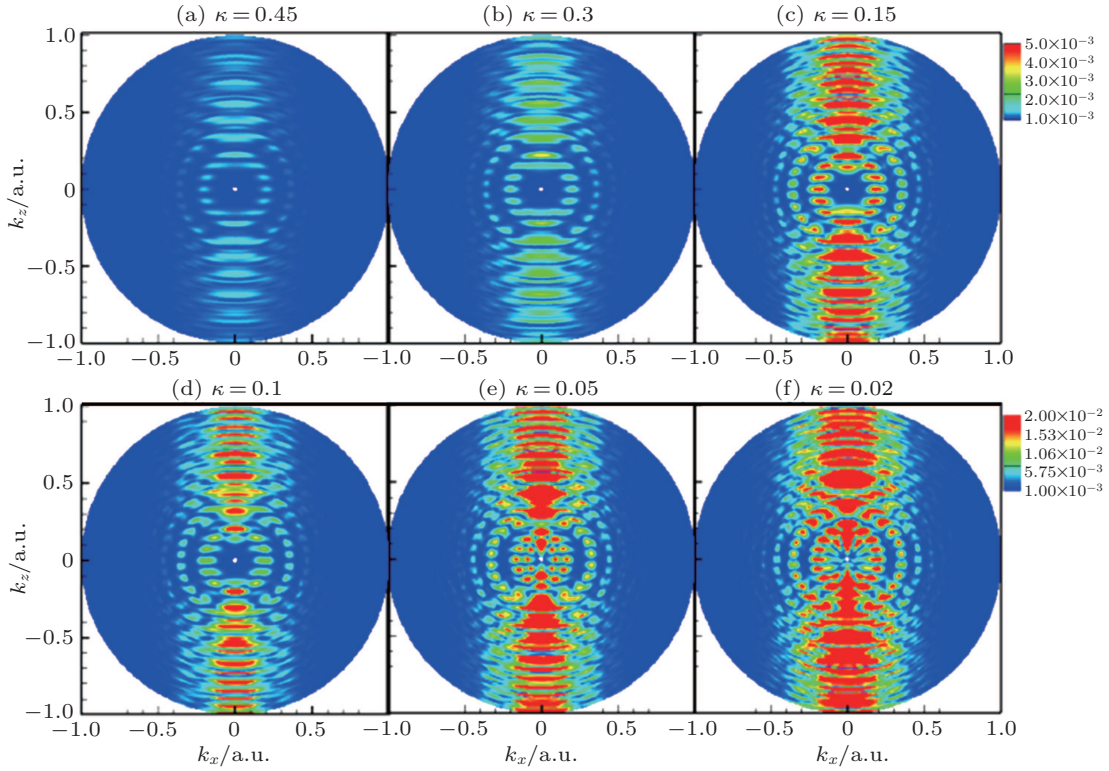


Fig. 5. (color online) The same as those in Fig. 4, for a different wavelength at 1005 nm. Here, (a) $\kappa = 0.45$, (b) $\kappa = 0.3$, (c) $\kappa = 0.15$, (d) $\kappa = 0.1$, (e) $\kappa = 0.05$, (f) $\kappa = 0.02$.

Table 2. The dominant angular momentumls for the first ATI ring.

κ/nm	0.45	0.3	0.1	0.05	0.02	Coulomb
996	2,4,6	4,6,8	4,6	4,6	6,8,10	6,8,10
1005	4,6	2,4,6	2,4,6	2,6	2,4,6,8	2,4,6,8,10

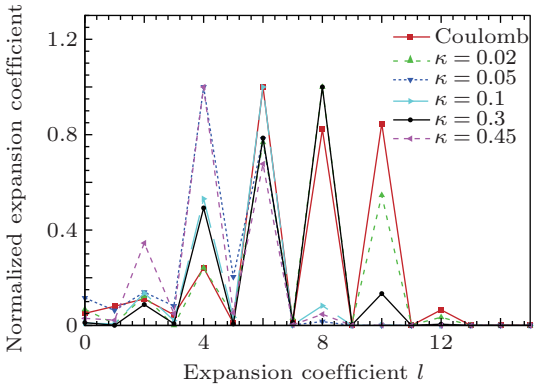


Fig. 6. (color online) The normalized expansion coefficients of the spherical harmonics for the momentum $\boldsymbol{k}$ on the first ATI ring of Fig. 4, calculated for $l = 0$ up to 15.

According to Eqs. (3) and (4), $P(\boldsymbol{k})$ can be further written as a linear combination of a series of spherical harmonic functions. The angular differential probability of the momentum is a reflection of the square of Legendre polynomial $[P_l(\cos\theta)]^2$ of different partial waves. We can obtain the dominant l for a certain k, and the spherical harmonics with different l determine the distribution on the PAD. Figure 6 is the expansion coefficients of the spherical harmonic with l no more than 15 for the momentum $\boldsymbol{k}$ on the first ring of Fig. 4. The dominant angular momentum ls is selected for whose expansion coefficients are on the largest order of magnitude. In Table 2, we show the dominant l on the first ring for 996 nm and 1005 nm in Figs. 4 and 5. The dominant l becomes large and disperse for the Coulomb potential and shows the interference of the electron wave packets is a combined effect of a series Rydberg states rather than one or a few excited states. The number of lobes of the PAD is not dominated by a certain angular momentum but a mixture of different angular momentums. From this, we can see the Rydberg states play an important role in the PAD and the intermediate transition cannot be omitted for investigating the fine structure in the momentum distribution.

4. Conclusion and perspectives

We theoretically investigate the low energy structure in the TI regime for different potentials at different laser parameters. By changing the wavelength, we find that the shift of the first ATI ring on the momentum distribution is consistent with the ionization modulation, which can be reproduced using both the Yukawa and the Coulomb potential. It is a result of the interference of wave packets emitted at different times, which reflects the nature of the laser field. The radial fan structure on the momentum distribution along with the number of lobes on the first ATI ring is greatly influenced by the atomic intermediate states. The long-range potential's influence is the Coulomb focusing effects and the generation of the "spider" structure along the laser's polarization direction. By changing the number of bound states in the Yukawa potential, we find that the radial shape of the lobes near the threshold is a result of resonant ionization while the number of the lobes is related to the combined effect of a series of Rydberg states.

References

[1] Keldysh L V 1964 *Zh. Eksp. Teor. Fiz* **47** 1945

[2] QuanW, Lin Z, Wu M, Kang H, Liu H, Liu X, Chen J, Liu J, He X T, Chen S G, Xiong H, Guo L, Xu H, Fu Y, Cheng Y and Xu Z Z 2009 *Phys. Rev. Lett.* **103** 093001

[3] Faisal F H M 2009 *Nat. Phys.* **5** 319

[4] Blaga C I, Catoire F, Colosimo P, Paulus G G, Muller H G, Agostini P and DiMauro L F 2009 *Nat. Phys.* **5** 335

[5] Huismans Y, Rouzée A, Gijsbertsen A, *et al.* 2011 *Science* **331** 61

[6] Bian X B, Huismans Y, Smirnova O, Yuan K J, Vrakking M J J and Bandrauk A D 2011 *Phys. Rev. A* **84** 043420

[7] Huismans Y, Gijsbertsen A, Smolkowska A S, Jungmann J H, Rouzée A, Logman P S W M, Lépine F, Cauchy C, Zamith S, Marchenko T, Bakker J M, Berden G, Redlich B, van der Meer A F G, Ivanov M Yu, Yan T M, Bauer D, Smirnova O and Vrakking M J J 2012 *Phys. Rev. Lett.* **109** 013002

[8] Hickstein D D, Ranitovic P, Witte S, Tong X M, Huismans Y, Arpin P, Zhou X, Keister K E, Hogle C W, Zhang B, Ding C, Johnsson P, Toshima N, Vrakking M J J, Murnane M M and Kapteyn H 2012 *Phys. Rev. Lett.* **109** 073004

[9] Arbó D G, Yoshida S, Persson E, Dimitriou K I and Burgdrfer J 2006 *Phys. Rev. Lett.* **96** 143003

[10] Arbó D G, Dimitriou K I, Persson E and Burgdrfer J 2008 *Phys. Rev. A* **78** 013406

[11] Marchenko T, Muller H G, Schafer K J and Vrakking M J J 2010 *J. Phys. B* **43** 095601

[12] Marchenko T, Muller H G, Schafer K J and Vrakking M J J 2010 *J. Phys. B* **43** 185001

[13] Li M, Liu Y, Liu H, Yang Y, Yuan J, Liu X, Deng Y, Wu C and Gong Q 2012 *Phys. Rev. A* **85** 013414

[14] Liu H, Liu Y, Fu L, Xin G, Ye D, Liu J, He X T, Yang Y, Liu X, Deng Y, Wu C and Gong Q 2012 *Phys. Rev. Lett.* **109** 093001

[15] Chen Z, Morishita T, Le A T, Wickenhauser M, Tong X M and Lin C D 2006 *Phys. Rev. A* **74** 053405

[16] Ammosov M V, Delone N B and Krainov V P 1986 *Sov. Phys. JETP* **64** 1191

[17] Delone N B and Krainov V P 1991 *J. Opt. Soc. Am. B* **8** 1207

[18] Paulus G G, Grasbon F, Walther H, Kopold R and Becker W 2001 *Phys. Rev. A* **64** 021401(R)

[19] Kopold R, Becker W, Kleber M and Paulus G G 2002 *J. Phys. B* **35** 217

[20] Freeman R R, Bucksbaum P H, Milchberg H, Darack S, Schumacher D and Geusic M E 1987 *Phys. Rev. Lett.* **59** 1092

[21] Peng LY, Pronin E A and Starace A F 2008 *New J. Phys.* **10** 025030

[22] Xu M H, Peng L Y, Zhang Z, Gong Q, Tong X M, Pronin E A and Starace A F 2011 *Phys. Rev. Lett.* **107** 183001

[23] Frolov M V, Knyazeva D V, Manakov N L, Popov A M, Tikhonova O V, Volkova E A, Xu M H, Peng L Y, Pi L W and Starace A F 2012 *Phys. Rev. Lett.* **108** 213002

[24] Song S N, Geng J W, Jiang H B and Peng L Y 2014 *Phys. Rev. A* **89** 053411

[25] Song S N, Geng J W, Li L Z, Jiang H B and Peng L Y 2015 *Phys. Rev. A* **91** 053401

[26] Geng J W, Xiong W H, Xiao X R, Peng L Y and Gong Q 2015 *Phys. Rev. Lett.* **115** 193001

[27] Wu C Y, Yang Y D, Liu Y Q, Gong Q H, Wu M, Liu X, Hao X L, Li W D, He X T and Chen J 2012 *Phys. Rev. Lett.* **109** 043001

[28] Huismans Y, Rouzée A, Gijsbertsen A, Logman P S W M, Lépine F, Cauchy C, Zamith S, Stodolna A S, Jungmann J H, Bakker J M, Berden G, Redlich B, van der Meer A F G, Schafer K J and Vrakking M J J 2013 *Phys. Rev. A* **87** 033413

[29] Bai L H, Zhang J T, Xu Z Z and Guo D S 2006 *Phys. Rev. Lett.* **97** 193002